RSC Advances

ROYAL SOCIETY OF CHEMISTRY

www.rsc.org/advances

RSC Advances

ARTICLE

Synthesis and characterization of micro/nano-structured $BaHPO_4$/$Ba_3(PO_4)_2$/$Ba_5(PO_4)_3OH$ and their luminescence

Miaohui Tong[a, b], Jianwen Zhao[b], Yujun Liang[a, b, *], Yingli Zhu[b], Xingya Wu[b], Shiqi Liu[b], Chunjie Yan[a, b], Guogang Li[a, b]

Microspheres sphered with microcuboids/nanorods and nanoparticles of $BaHPO_4$/$Ba_3(PO_4)_2$/$Ba_5(PO_4)_3OH$ phases have been successfully synthesized by a facile hydrothermal (HT) method using citric acid as the surfactant at different pH values. X-ray diffractometer (XRD), field emission scanning electron microscope (FE-SEM) and fluorescence spectrometer were used to characterize the samples. It was found that the pH value was a crucial factor for phase forming and shape determination of final products, which were discussed in detail. Attractively, the as-prepared $BaHPO_4$/$Ba_3(PO_4)_2$/$Ba_5(PO_4)_3OH$ samples emitted an intense blue light in a broad band from 380 to 625 nm, of which the mechanism was the complex ions luminescence originating from the transition of $^3T_1 \rightarrow {}^1A_1$ in PO_4^{3-}. Meanwhile, an obvious red shift for the emission band was observed between nano- and bulk-$Ba_3(PO_4)_2$ synthesized by the HT and conventional solid-state reaction (CSS), respectively, which was due to the effect of nanometer-size. The same effect was also shown up as a result of the fact that the decay time of the latter was about 2.5 times of that of the former. Moreover, the decay mode of $Ba_5(PO_4)_3OH$ was different from those of $BaHPO_4$ and $Ba_3(PO_4)_2$, which was ascribed to the effect of the substitution of three OH^- for one PO_4^{3-} on their electronic structures.

1. Introduction

In the past tens of years, the orthophosphates of barium, $Ba_3(PO_4)_2$, has been reported to be a good host for rare earths doped luminescence materials. In the early year of 1979, Tale et al. reported that Eu^{2+} doped $Ba_3(PO_4)_2$ was an efficient luminophor for X-ray screens[1]. Subsequently, Poort et al. published their researched results in 1996 that the emission spectrum of $Ba_3(PO_4)_2$:Eu^{2+} presented two blue bands ascribed to two different positions of Eu^{2+} in the host[2]. In 2003, Liang et al. systematically investigated the optical spectroscopic properties of Ce^{3+}, Sm^{3+}, Eu^{3+}, Eu^{2+} and Tb^{3+} doped $Ba_3(PO_4)_2$[3]. For further researches, in 2011, Chen et al. studied the luminescence properties of Ce^{3+} and Dy^{3+} ions co-doped $Ba_3(PO_4)_2$[4]. They found that the introduction of a moderate amount of Dy^{3+} ions could cause a red shift of Ce^{3+} emission band and enhance its emission intensity. However, the CSS route has been the only preparation method for all these phosphors. As we all know, block-shape and bad particle distribution are prominent disadvantages of CSS products, which may be not good to the phosphors. In addition, long sintering time and high sintering temperature in CSS process greatly increase the cost. To improve the current situation, soft chemical synthetic method, including sol-gel, precipitation and HT synthesis and so on[5, 6], has been rapidly developed and certified to be one of the most effective and convenient

approaches to yield homogeneous and shape-controllable products with micro/nanostructures in recent years[7, 8]. In 2012, Cheng et al. successfully synthesized Eu^{2+} and Tb^{3+} doped $Ba_3(PO_4)_2$ nanowires by precipitation method for the first time, but the anodic aluminum oxide was used as a template in the precipitation process, which involved a complicated process and might introduce the impurities owing to the incomplete removal of the template[5, 9, 10]. As such, template-free strategies should be more popular, among which HT synthesis is a typical one. In HT condition, a unique trait is that the liquid or gas is usually used as the reaction medium in a closed environment to form a high temperature and high pressure surroundings, which can promote the formation of well-dispersed and good-shaped crystals with complete crystallization by one step[11, 12]. Many experiments showed that the shape and phase structure of products depended on the HT conditions on a certain degree, including pH value of the initial solution, the type and amount of surfactant, reaction time and temperature, and the concentration of reaction solution etc.[8, 13-17]. Therefore, this present work focuses on the HT process in the synthesis of $Ba_3(PO_4)_2$ materials. It is exciting that different phases, with kinds of basic elements assembled spheres, were formed under different pH values, and all of the as-obtained host materials was observed to show an intense blue emitting for the first time. Moreover, some nanostructures were generated in the HT process, which demonstrated different luminescence properties

compared with CSS products. This finding that all of the as-synthesized non-rare earths doped $BaHPO_4/Ba_3(PO_4)_2/Ba_5(PO_4)_3OH$ materials emit a blue light in our work may contribute to near-ultraviolet (n-UV) conversion tri-color phosphors and save rare earth resources on some degree.

2. Experimental

2.1. Synthesis. The $Ba_3(PO_4)_2$ powder was expected to be obtained by HT method at the beginning. The raw materials were $Ba(NO_3)_2$ (A.R.) and $NH_4H_2PO_4$ (A.R.). In a typical procedure, the stoichiometric amount of $Ba(NO_3)_2$ and $NH_4H_2PO_4$, and moderate citric acid (CA) acting as a surfactant were weighed and dissolved together in deionized water under continuous stirring. Subsequently, ammonia ($NH_3 \cdot H_2O$) was added to adjust the pH at different values. After additional agitation for 30 minutes, the mixed solution was transferred to an autoclave with 30% filling capacity followed by a HT treatment under the condition of 180℃ for 12 h. The as-obtained samples were washed several times by deionized water and anhydrous ethanol, then dried in an oven at 80℃. As a comparison, the $Ba_3(PO_4)_2$ samples were also synthesized by CSS reaction added with 0 and 5 mass% H_3BO_3 (labelled as CSS0 and CSS5), respectively. As raw materials, the stoichiometric amount of $BaCO_3$ and $NH_4H_2PO_4$ were weight and mixed well in an agate mortar. The mixture was then transferred to an alumina crucible and calcined at 1300℃ for 4 h in an oxygen atmosphere. Finally, the as-obtained samples were slowly cooled to room temperature for subsequent characterization.

2.2. Characterization. The crystal structure of the phosphors was characterized by X-ray diffractometer (XRD) (Bruker D8 Focus) with Ni-filtered Cu-Kα (λ = 1.540598 Å) radiation at 40 kV tube voltage and 40 mA tube current. The XRD data were collected in a 2θ range from 10° to 70°, with the continuous scan mode at the speed of 0.05 s per step with step size of 0.01°. The morphology and microstructure were characterized with Japan SU8010 field emission scanning electron microscope (FE-SEM) at 15 kV. Excitation and emission spectra were measured by fluorescence spectrometer (FLUOROMAX-4P, Horiba Jobin Yvon, New Jersey, USA) equipped with a 150 W xenon lamp as the excitation source. The spectral step length of both excitation and emission spectra was set up to be 1.0 nm with the width of the monochromator slits adjusted as 0.50 nm. The lifetime was recorded on a spectro-fluorometer (HORIBA, JOBIN YVON FL3-21), and the pulse laser radiation (nano-LED) was used as the excitation source. The other measurement conditions were kept consistent from sample to sample in measurements. All the measurements were carried out at room temperature.

3. Results and discussion

3.1. Phase identification, structure and calculation of crystallite size. Figure 1 shows the as-obtained phases by a HT process at 180℃ for 12 h with different pH values of 6.0, 7.0, 8.0, 9.0 and 10.0. For comparison, XRD standard data patterns of the Joint Committee on Powder Diffraction Standards (JCPDS) card no. 72-1370 and 78-1141 are synchronously given. It could be found that $BaHPO_4$ was obtained with the pH value adjusted as 6.0, 7.0, 8.0 and 9.0, respectively, and further elevating the pH value to be 10.0, $Ba_5(PO_4)_3OH$ could be formed. These results
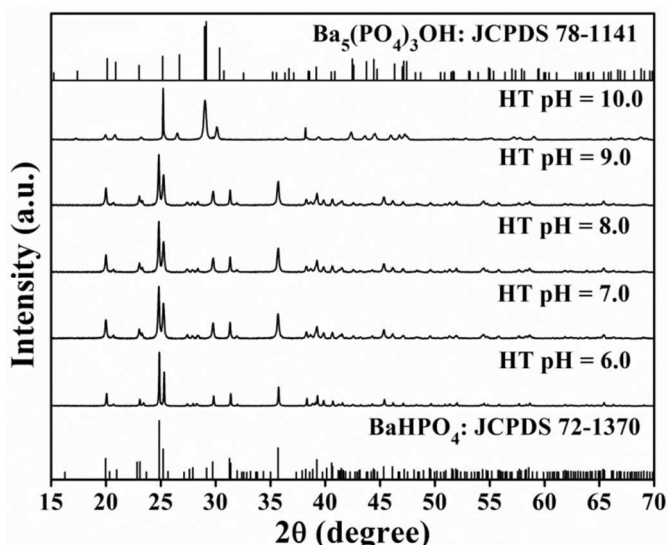

Figure 1 XRD data of the as-synthesized samples by HT method under 180℃ for 12 h at different pH values together with the standard data of $BaHPO_4$ (JCPDS card no. 72-1370) and $Ba_5(PO_4)_3OH$ (JCPDS card no. 78-1141) as references.

suggest that the pH value has much effect on the phase forming while other experimental conditions are the same, thus we assume that $Ba_3(PO_4)_2$ should be obtained by adjusting the pH values to be 9.0 ~ 10.0 as shown in Figure 2, in which the XRD data of as-synthesized CSS0 and CSS5 samples prepared through a high temperature solid state process at 1300℃ for 4 h under an atmosphere, together with the JCPDS card no. 85-0904, are demonstrated. As expected, the $Ba_3(PO_4)_2$ phase was obtained under feasible conditions, which was exactly indexed to the pure trigonal phase belonging to the space group R-3m (No. 166) with cell parameters of a = b = c = 7.711 Å, V = 570.28 Å^3, and Z = 1.

Among the as-synthesized $Ba_3(PO_4)_2$ samples, the relative intensities of diffraction peaks obtained under HT condition were stronger than that under CSS condition. Moreover, between CSS0 and CSS5, the relative intensities of the former were weaker than the latter. The integrity of crystallization under different reaction conditions may be responsible for these results[16]. As mentioned above, the surroundings in a closed environment under HT condition is better than that in CSS to generate high crystallization products. And in CSS process, H_3BO_3, a powdered solid at room temperature, will melt into liquid at about 169℃, thus a liquid surroundings is created, which can provide more contact room for solid-state raw materials of $BaCO_3$ and $NH_4H_2PO_4$ so that they have sufficient mixing to react better[18-20]. And finally, in comparison to CSS with 0% H_3BO_3 (CSS0), powders with better crystallization (CSS5) can be obtained.

On the other hand, for the three typical samples obtained by HT method, it was observed that the differences in relative intensities based on (110) and (205) were especially salient, which were due to the different preferential orientation growth caused by different pH values[5, 21, 22]. The similar phenomenon could also be found in the as-prepared samples using CSS method, which, however, was probably ascribed to the introduction of H_3BO_3.

Also note that the full width at half maximum (FWHM) of diffraction peaks for the three typical $Ba_3(PO_4)_2$ samples

synthesized in HT condition has been widen compared with those in CSS condition as illustrated in Figure 2(b). Generally speaking, when one crystallite size is larger than 200 nm, the FWHM of diffraction peaks will be kept as a constant which just only depends on the instrument (Bruker D8 Focus XRD in our work), conversely, it will be broaden due to the incomplete coherent scattering. Herein, the phenomenon shown in Figure 2(b) indicates that the average crystallite sizes of as-prepared $Ba_3(PO_4)_2$ samples under HT condition are at nanometer scale smaller than 200 nm, which can be theoretically estimated by the Scherrer equation[23-25] as follows:

$$D_{hkl} = \frac{k\lambda}{\beta(2\theta)\cos\theta} \quad (1)$$

where k is a constant of 0.89, λ is the wavelength of the X-rays (0.15405 nm), $\beta(2\theta)$ is FWHM of the considered diffraction peak in radian after correcting for instrumental peak's broadening, θ is the Bragg angle (half of the diffraction angle 2θ), and D_{hkl} is the size of the crystallite which is perpendicular to the plane (hkl). For the samples synthesized at the pH value of 9.3 (HT9.3), 9.5 (HT9.5) and 9.7 (HT9.7), respectively, the average crystallite sizes were estimated to be 71, 66 and 63 nm. It suggests that the average crystallite size gradually dwindles with the pH value increasing, which will be verified by SEM experimental results.
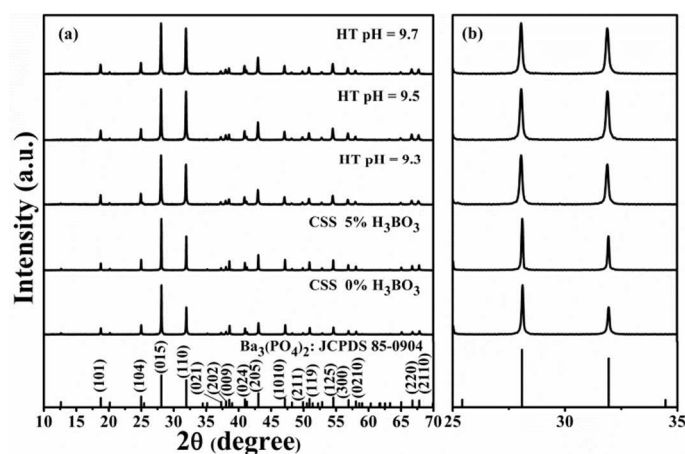

Figure 2 (a) XRD data of as-synthesized samples via CSS route at 1300℃ for 4 h under an oxygen atmosphere and HT method at 180℃ for 12 h with different pH values. The standard datum of $Ba_3(PO_4)_2$ (JCPDS card no. 85-0904) is used as a reference. (b) Partially enlarged details of XRD patterns to show the differences of the major peaks.

3.2. Phase forming, morphology and growth scheme. It has been found that the pH value acts as an important role in the phase structure of the as-formed samples in HT route, which may also have effects on the morphologies. Figure 3 demonstrates the SEM images of the final samples obtained at 180℃ for 12 h under different pH values. On the general, they are micro-/nano-structured materials with some differences in morphology. The XRD results indicate that the $BaHPO_4$ phase can be obtained under HT condition with the pH value at 6.0, 7.0, 8.0 and 9.0, respectively, of which the morphologies are all microspheres with different sizes and structural components. Figure 3(A) and (B) show the shapes of $BaHPO_4$ samples obtained with the pH value at 6.0. The homogenous flower-like

microspheres were petalled by a large number of uneven micro-cuboids which coincidentally spread outward from the center of flowers. As the pH value was gradually increased to be 7.0, 8.0 and 9.0, a series of microspheres with different sizes were observed in Figure 3(C), (E) and (G), respectively. From the corresponding higher magnification SEM images (D), (F) and (H), it could be seen that the petals of flower-like microspheres seemed to be variable with respect to that shown in image (B), in which orderly slender nanorods, circular planes formed with
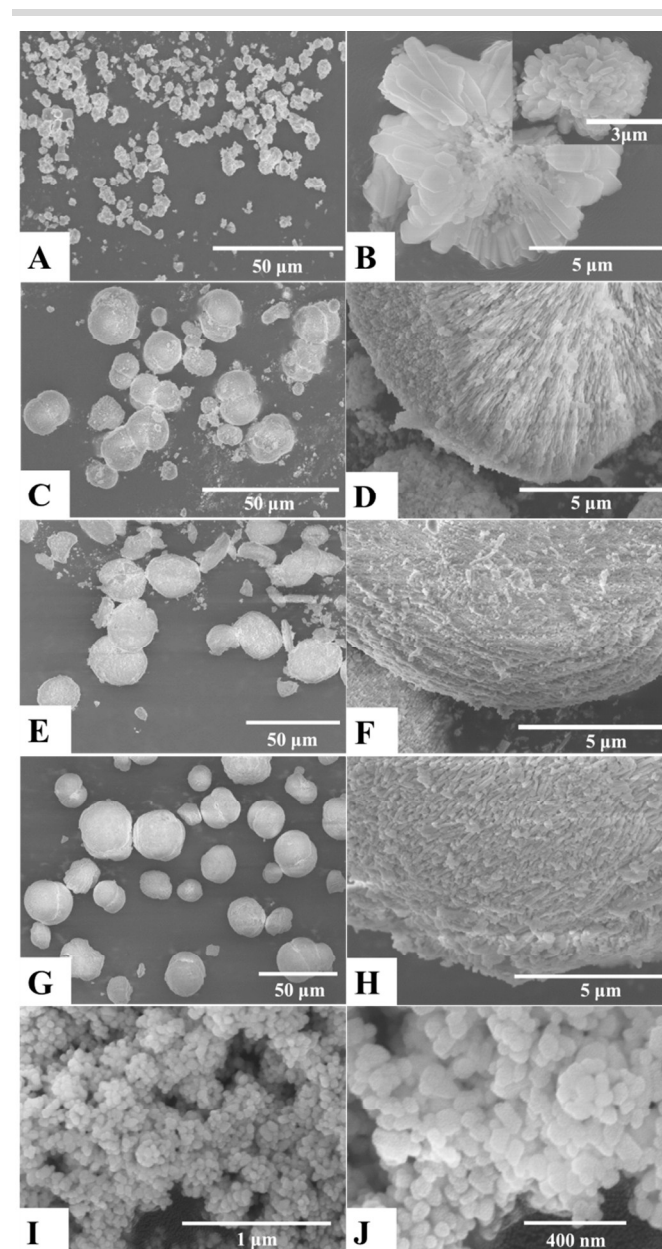

Figure 3 SEM images of as-synthesized samples under HT conditions at 180℃ for 12 h with the pH value at (A and B) 6.0: flower-like microspheres petalled with microcuboids, (C and D) 7.0: microspheres sphered with orderly nanorods, (E and F) 8.0: microspheres/hemispheres constructed by a series of planes formed with aggregated nanorods, (G and H) 9.0: microspheres structured with messy and aggregated nanorods, and (I and J) 10.0: nanoparticles.

aggregated nanorods and, messy and aggregated nanorods were respectively observed to be the basic constituent elements of those microspheres. Increasing the pH value to be 10.0, the as-formed nanoparticles were the phase of $Ba_5(PO_4)_3OH$, however. Further accurately adjusting the pH value between 9.0 and 10.0, an expected phase, $Ba_3(PO_4)_2$, was yielded. Figure 4-1 exhibits the SEM images of $Ba_3(PO_4)_2$ samples prepared with the pH
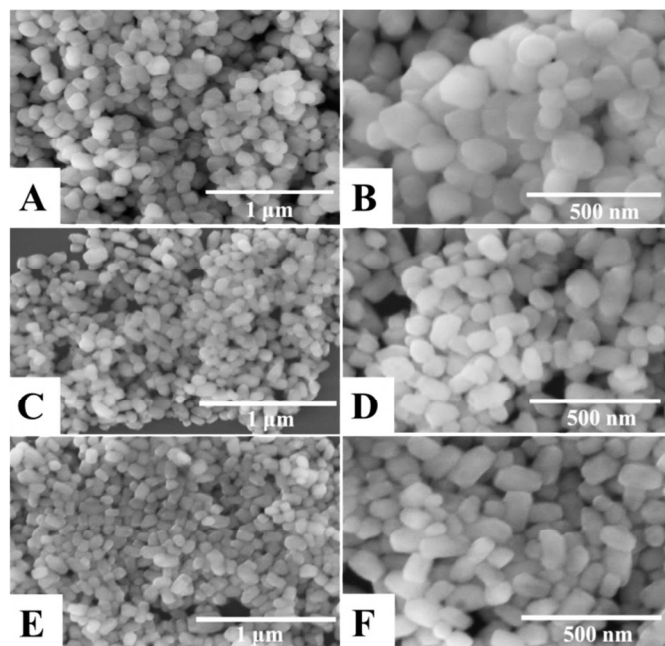

Figure 4-1 SEM images of as-prepared $Ba_3(PO_4)_2$ samples by HT method at 180℃ for 12 h under different pH values: (A and B) non-uniform round-granular nanoparticles at pH = 9.3, (C and D) mixture of long- and round-granular nanoparticles at pH = 9.5, and (E and F) long-granular nanoparticles at pH = 9.7.
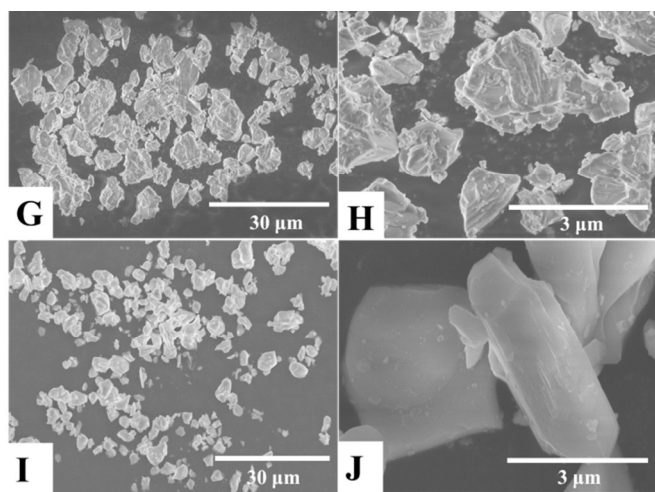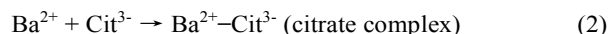

Figure 4-2 SEM images of as-obtained $Ba_3(PO_4)_2$ samples by CSS method added with (G and H) 0 mass% H_3BO_3 (CSS0): heterogeneous, irregular and shaggy bulks, and (I and J) 5 mass% H_3BO_3 (CSS5): less heterogeneous, regular and smooth bulks.
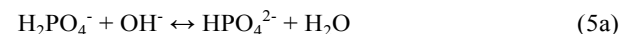
value at 9.3 (A and B), 9.5 (C and D) and 9.7 (E and F), respectively. As depicted in Figure 4-1(A), (C) and (E), the as-prepared $Ba_3(PO_4)_2$ samples were composed of good distribution nanoparticles, of which the size gradually decreased with the pH value ranging from 9.3 to 9.7. Comparing the further amplification images (B), (D) and (F), it was revealed that the shapes of particles trended to convert round to long, which confirmed the phenomenon of different preferential orientation growth from the perspective of morphology. Moreover, all these nanoparticles presented a very smooth surface indicating the good crystallinity as what XRD results had clarified[26]. Of all the as-prepared samples, the possible phase structure formation mechanism, accompanied with morphology architecture details, is shown in Scheme 1. It highlights the roles of both the pH value and CA in phase formation and morphologies of the final products. The whole process may be described with the following equations.

$$Ba^{2+} + Cit^{3-} \rightarrow Ba^{2+}-Cit^{3-} \text{ (citrate complex)} \qquad (2)$$

$$HPO_4^{2-} + H_3O^+ \leftrightarrow H_2PO_4^- + H_2O \leftrightarrow H_3PO_4 + OH^- \qquad (3)$$

(Add $NH_3 \cdot H_2O$ into the above solution system)

$$NH_3 \cdot H_2O \leftrightarrow NH_4^+ + OH^- \qquad (4)$$

pH = 6.0 ~ 9.0,

$$H_2PO_4^- + OH^- \leftrightarrow HPO_4^{2-} + H_2O \qquad (5a)$$

$$Ba^{2+}-Cit^{3-} + HPO_4^{2-} \rightarrow BaHPO_4 + Cit^{3-} \qquad (5b)$$

pH = 9.0 ~ 10.0,

$$H_2PO_4^- + 2OH^- \leftrightarrow PO_4^{3-} + 2H_2O \qquad (6a)$$

$$Ba^{2+}-Cit^{3-} + PO_4^{3-} \rightarrow Ba_3(PO_4)_2 + Cit^{3-} \qquad (6b)$$

pH = 10.0,

$$3H_2PO_4^- + 7OH^- \leftrightarrow [(PO_4)_3OH]^{10-} + 6H_2O \qquad (7a)$$

$$Ba^{2+}-Cit^{3-} + [(PO_4)_3OH]^{10-} \rightarrow Ba_5(PO_4)_3OH + Cit^{3-} \qquad (7b)$$
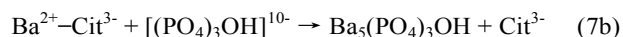
The citrate complex ($Ba^{2+}-Cit^{3-}$) is temporarily formed by an absorption process when cationic Ba^{2+} meets with CA, which then waits for the right anion to take the Ba^{2+} ions away. Know that $H_2PO_4^-$, H_3PO_4 and HPO_4^{2-} exist synchronously in $NH_4H_2PO_4$ aqueous solution as shown in equation (3), and adding moderate amount of $NH_3 \cdot H_2O$ will change the balance system. The OH^- in $NH_3 \cdot H_2O$ aqueous solution can restrain the right side reaction while accelerating the left one resulting in the less and less H_3PO_4. In our case, when the pH value was adjusted to be 6.0~9.0, HPO_4^{2-} became to be the selective anion that conducted an ion-exchange reaction with citrate ions to generate $BaHPO_4$ phase as represented in equation (5a) and (5b). Likewise, when the OH^- concentration was appropriately accommodated in the reaction system, the phases of $Ba_3(PO_4)_2$ and $Ba_5(PO_4)_3OH$, could be obtained, respectively, exactly as equation (6a) and (6b), (7a) and (7b) said. Throughout the process, various morphologies of products were formed by the way, which were illustrated in Scheme 1(b). Under different pH

conditions, Cit^{3-} emerged different absorption/desorption abilities that could control the reaction rates to yield products with various morphologies and sizes in the same limited reaction time[13, 27]. On the other hand, CA has three carboxylic groups and each of them stretches to an unique spatial orientation, which will be highly sensitive to the surface's molecular structure named face-specific. Hence, it could assemble the pre-grown elementary structures (microcuboids, nanorods and nanoparticles) together by binding sideways to each other and, in view of growth energies, the new crystal nucleus prefer to develop on the existing growth steps to form the final flower-like structures, spheres and aggregated round-/long-particles[8, 13, 27-29]. Turning to the fact that the $Ba_3(PO_4)_2$ crystallite size decreases with the pH value increasing from 9.3 to 9.7, the citrate complex $Ba^{2+}-Cit^{3-}$ and OH^- concentration have comprehensive actions. As the equation (6a) shows, the increasing OH^- concentration will destroy the reaction balance system and promote the right reaction to produce more PO_4^{3-}, which will immediately react with $Ba^{2+}-Cit^{3-}$ as demonstrated in equation (6b) to form more and more $Ba_3(PO_4)_2$ crystal nuclei before the initially formed $Ba_3(PO_4)_2$ crystal nuclei grow
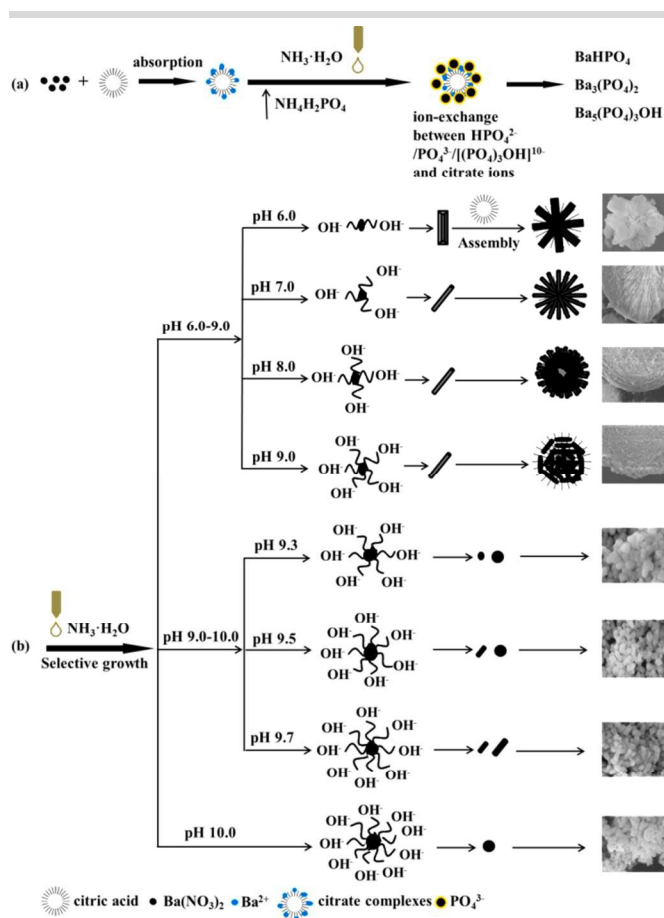
Scheme 1 The possible schematic illustration for the forming process of as-obtained HT products under different pH values at 180℃ for 12 h. (a) To clarify the reaction process, (b) to unfold the forming details of phases and morphology structures. The whole process can be concluded as (1) to form Ba^{2+}-citrate complex, (2) ion-exchange between PO_4^{3-} and citrate, meanwhile, OH^- ions come to effect, and (3) to assemble (pH value at 6.0-9.0) with unit elements[13, 26].
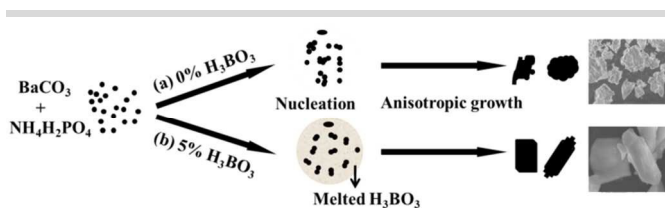
Scheme 2 Forming schematic for morphologies of the as-prepared $Ba_3(PO_4)_2$ samples by CSS method added with (a) 0 mass% H_3BO_3: direct solid-solid boundaries, aggregation nucleation to form irregular and shaggy blocks without liquid surroundings, and (b) 5 mass% H_3BO_3: sufficient mixing, the less direct solid-solid boundaries and homogeneous nucleation to form smooth and well-dispersed particles in liquid environment[18, 30].

up. According to the growth route, the $Ba_3(PO_4)_2$ nanoparticles with smaller size can be obtained when the pH value increases.

Moreover, the SEM images of $Ba_3(PO_4)_2$ samples prepared by CSS method, added with extra 0 (G and H) and 5 mass% (I and J) H_3BO_3, are revealed in Figure 4-2. It gave off the signal that, regular and smooth blocks with good distribution could be achieved with additional 5 mass% H_3BO_3 added in the raw materials while irregular and shaggy blocks were observed without H_3BO_3 in, which implied that proper amount of H_3BO_3 could work as a "shape modifier" like organic additive to improve the crystallization, shape and surface smoothness. The possible influencing mechanism is illustrated in Scheme 2. In the growth process, H_3BO_3 melts into liquid phase promoting mobility and homogeneity of solid reactants to gain products with less surface defects on one hand, and eliminating the aggregation of solid-solid contact to from well-dispersed particles on the other hand[18, 19, 31].

Comparing Figure 4-1 with 4-2, an emphasis should be focused on it that the particle sizes of as-synthesized $Ba_3(PO_4)_2$ samples using different methods were at different measure level. Obviously, the size of products obtained by HT was at nanoscale while that by CSS was at micron level. The difference in size level may have a big influence on luminescence properties of $Ba_3(PO_4)_2$ as reported in ZnO case previously[32, 33].

3.3. Luminescence properties and mechanism. Figure 5 exhibits the photoluminescence excitation and emission spectra of the series of as-synthesized samples by CSS and HT methods, respectively. As found from Figure 5(a) and (b), $Ba_5(PO_4)_3OH$, $Ba_3(PO_4)_2$ and $BaHPO_4$ samples, which were obtained using HT method under the pH value of 10.0, 9.5 and 8.0, respectively, demonstrated similar profiles in both excitation and emission spectra with different peaks and relative intensities. Moreover, according to the phase order of $Ba_5(PO_4)_3OH$, $Ba_3(PO_4)_2$ and $BaHPO_4$, blue shifts of 2-5 nm could be observed in their emission spectra with the peak at 447, 444 and 442 nm correspondingly. In essence, all these differences may result from the different phase structures.

As for the as-formed $Ba_3(PO_4)_2$ phase via CSS and HT method, respectively, there are many differences in photoluminescence properties. The excitation spectra in Figure 5(a) illustrate that, the excitation spectrum of $Ba_3(PO_4)_2$ prepared by CSS was composed of two broad bands from 225 to 400 nm with the intense peak at 320 nm while that approached by HT presented only a broad band from 250 to

420 nm centred at 376 nm, between which an obvious red shift of 56 nm existed. At the same time, a similar fact could also be found in their emission spectra as shown in Figure 5(c), which said that the emission peaks of as-obtained $Ba_3(PO_4)_2$ samples by CSS and HT route were at 414 and about 444 nm, respectively. The photoluminescence spectra show that the as-prepared blue emission $Ba_3(PO_4)_2$ phosphor can be applied to the white light emitting method of n-UV conversion tri-color phosphors. Also note that the FWHM of emission peaks for $Ba_3(PO_4)_2$ samples by HT have been broaden and the relative intensities were higher in comparison to those by CSS, which were consistent with the XRD results. Moreover, a new sharp emission peak at 403 nm could be observed in the emission spectrum of $Ba_3(PO_4)_2$ synthesized by HT route. All these phenomena may ascribe to the size achieving at the nanometer scale. As we all know, small size effect, surface and interface effect, quantum size effect, macroscopic quantum tunnel effect and dielectric confinement effect are the five main specific effects of nanomaterials, among which the first two are research emphasis for their effects on luminescence properties[34, 35]. Generally, red shifts are probably assigned to the surface and interface effect. In detail, the surface tension of nanoparticles will increase due to the surface and interface effect, which could increase the crystal field leading to energy levels to change or the narrowing of band gap. And the small size effect can generate two results. With the decreasing sizes of nanomaterials, the crystal periodic boundary conditions will be destroyed to introduce unordered phase resulting in the broadening of emission peaks on one hand. And on the other hand, the relevant specific surface area will increase promptly, which puts numerous surface atoms at exposed state so that many surface defects are inevitable. Herein, the spectral composition may change, such as the observed new sharp absorption peak in our case. In nanometer scale, material's properties are highly sensitive to the particle sizes. With increasing the pH value from 9.3 to 9.7 under HT condition,
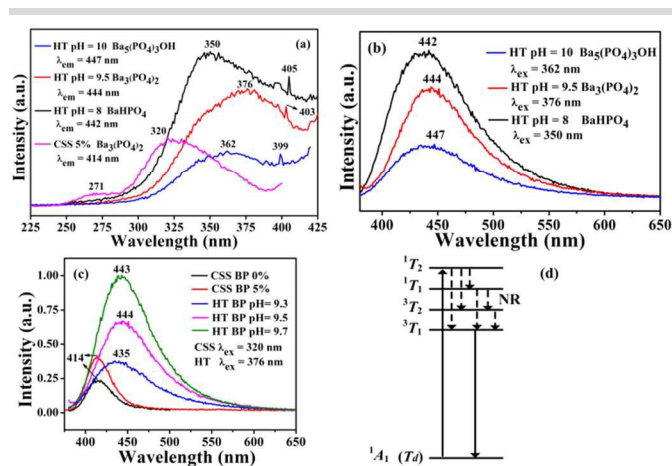
Table 1 A summary of emission peak, FWHM, relative intensities and particle size for the as-synthesized $Ba_3(PO_4)_2$ samples by CSS and HT routes, respectively.

$Ba_3(PO_4)_2$ samples prepared under CSS and HT conditions	Emission peak (nm)	FWHM (nm)	Relative intensity (a.u.)	Particle size (nm)
CSS 0% H_3BO_3	414	33.44	0.2329	–
CSS 5% H_3BO_3	414	34.52	0.4095	–
HT pH = 9.3	435	78.53	0.3778	71
HT pH = 9.5	444	76.35	0.6745	66
HT pH = 9.7	443	72.91	1.0015	63

there were gradual increase in the relative intensities and narrowing in the FWHM for $Ba_3(PO_4)_2$ samples as listed in Table 1. From the results of XRD in Figure 2, it could be seen that the diffraction intensities, especially along the plane (110) and (205), slowly increased according to the sample sequence of HT9.3, HT9.5, and HT9.7, which implied the better and better crystallinity of particles with increasing the pH value from 9.3 to 9.7. Combining the above results, it is concluded that particles with better crystallinity show higher emission intensities in our current work, which can also be used to interpret the phenomenon of the stronger relative intensity of CSS5 (added with 5 mass% H_3BO_3) than CSS0 (without H_3BO_3) in CSS condition. Synchronously, all these phenomena can be supported by SEM results of surface smoothness and good graininess.

The photoluminescence mechanism of as-prepared $BaHPO_4$, $Ba_3(PO_4)_2$ and $Ba_5(PO_4)_3OH$ hosts can be explained similar to that of MoO_4^{2-} [36], WO_4^{2-} [37] and VO_4^{3-} [38, 39] by the model of the MO_4^{n-} (n = 1, 2, 3 and 4) complex due to the common closed-shell electronic configurations, which is one of the common four kinds of luminescence centers, namely, ns^2 type, transition metal, lanthanide metal and complex ions luminescence centers[40]. Actually, the outer electron configuration of P atom is $3s^23p^3$, and in our case, unequal four sp^3 hybrid orbitals are formed when bonding with O atom, of which the one occupied by a pair of electrons has lower energy and the other three, respectively occupied by a single electron, have higher energy so that a coordination bond and three covalent bonds come into being between P and O. Therefore, the [PO4] group is a deformation tetrahedron with P as the center. Based on the above discussion, P^{5+} ion has a closed-shell electronic configuration with an empty $3d$ orbital in PO_4^{3-}. Corresponding to the electron charge-transfer transition process from the O2p orbital (t_1 symmetry in T_d) to the 3d orbital (e and t_2 symmetry) of the P^{5+} ion, a broad blue band ranging from 380 to 625 nm was observed when excited. To make the luminescence process clearer, the molecular orbital theory[41] is usually used. A molecular orbital calculation leads to e and t_1 states for the lowest unoccupied molecular orbital (LUMO) and the highest occupied molecular orbital (HOMO), respectively. By taking the $e \rightarrow t_1$ transition into account, the excited electronic states of t_1e electronic configuration in T_d symmetry are found to consist of $^3T_1 \cong {}^3T_2 < {}^1T_1 < {}^1T_1$ in the order of increasing energies, the ground state being a $^1A_1$ state. The orbital triplets ($^3T_1$, $^3T_2$) have degenerate levels in the spectral region of 250 to

Figure 5 (a) Excitation spectra of $Ba_3(PO_4)_2$ sample prepared by CSS method added with 5 mass% H_3BO_3, and samples of $Ba_5(PO_4)_3OH$, $Ba_3(PO_4)_2$ and $BaHPO_4$ obtained by HT route at pH value of 10, 9.5 and 8 respectively. (b) Emission spectra of $Ba_5(PO_4)_3OH$, $Ba_3(PO_4)_2$ and $BaHPO_4$. (c) Emission spectra of a series of $Ba_3(PO_4)_2$ samples synthesized by CSS (with 0 and 5 mass% H_3BO_3) and HT (pH = 9.3, 9.5 and 9.7) methods, respectively. (d) Energy scheme for luminescence process of PO_4^{3-} molecule.

500 nm. Herein, Figure 5(d) gives the three-level energy scheme for luminescence process of PO_4^{3-} molecule. Since the photoluminescence properties of nano-samples achieved under HT condition will have some changes, CSS-yielded $Ba_3(PO_4)_2$ sample is used to illustrate the luminescence process of PO_4^{3-}, which can be described as the following in detail. Combining Figure 5(a), (c) and (d), when pumped by 271/320 nm, electrons can be excited from the ground state $^1A_1$ to the excited states $^1T_2/^1T_1$, following a non-radiative (NR) transition process among the excited states of PO_4^{3-} electrons are then transferred to $^3T_1$, and finally electrons return to the ground state and give the emission of PO_4^{3-} ion centred at 414 nm.
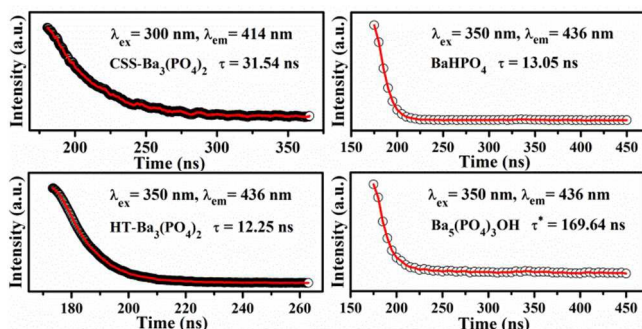

Figure 6 Decay curves of host emissions for samples obtained via HT method ($BaHPO_4$, $Ba_3(PO_4)_2$ and $Ba_5(PO_4)_3OH$) and CSS method ($Ba_3(PO_4)_2$), respectively.

Figure 6 depicts the decay curves of as-prepared hosts $BaHPO_4$, $Ba_3(PO_4)_2$ and $Ba_5(PO_4)_3OH$. The decay curves of $BaHPO_4$ and $Ba_3(PO_4)_2$ were well fitted with a typical single-order exponential decay mode as equation (8)[42] while that of $Ba_5(PO_4)_3OH$ was a second-order as equation (9)[43].

$$I(t) = I_0 \exp(-t/\tau) \qquad (8)$$

$$I(t) = I_0 + A_1 \exp(-t/\tau_1) + A_2 \exp(-t/\tau_2) \quad (9)$$

$$\tau^* = (A_1\tau_1^2 + A_2\tau_2^2)/(A_1\tau_1 + A_2\tau_2) \qquad (10)$$

where I_0 expresses the initial emission intensity immediately after being excited, $I(t)$ is the luminescence intensity at time t; A_1 and A_2 are the fitting constants, and τ_1 and τ_2 are the decay times for the corresponding component. Based on the above equation (8) and (9), the average decay times were determined to be 13.05, 12.25 and 31.54 ns for $BaHPO_4$, HT-$Ba_3(PO_4)_2$ and CSS-$Ba_3(PO_4)_2$ (HT/CSS-$Ba_3(PO_4)_2$ denotes the sample generated by HT/CSS route), respectively, and that of $Ba_5(PO_4)_3OH$ could be calculated by equation (10)[37], which was 169.64 ns. Firstly, the decay time of CSS-$Ba_3(PO_4)_2$ is about 2.5 times of that of HT-$Ba_3(PO_4)_2$. That is, the decay time of nano-$Ba_3(PO_4)_2$ shorten dramatically compared with that of bulk-$Ba_3(PO_4)_2$, which may be ascribed to the increasing quenching centers on nanomaterial's surface resulting from interface and surface effect[35, 43, 44]. Secondly, we can note that the decay times of $BaHPO_4$ and HT-$Ba_3(PO_4)_2$ are almost the same while that of $Ba_5(PO_4)_3OH$ is about 12 times larger than them even though the spectral compositions are the same with respect to nano-$BaHPO_4$, -$Ba_3(PO_4)_2$ and -$Ba_5(PO_4)_3OH$. These phenomena demonstrate that the change of anionic groups can accordingly lead to the change of decay times further to certify that the main luminescence center comes from the [PO_4] group for the three hosts ignoring their different structures. Know that trigonal $Ba_3(PO_4)_2$, orthorhombic $BaHPO_4$ and hexagonal $Ba_5(PO_4)_3OH$ in our work have different electronic structures so that electrons should accordingly have different transition probabilities from the excited state to ground state, which put up various lifetimes. It is worth carrying out that the change of decay mode and the big difference in lifetime between nano-$Ba_3(PO_4)_2$ and -$Ba_5(PO_4)_3OH$ predict the big impact of the substitution of three OH^- for one PO_4^{3-} on the electronic structures or transition probability, which needs to be explored further.

4. Conclusions

In summary, this work has revealed a facile HT route for the synthesis of a series of micro-/nano-materials of $BaHPO_4$, $Ba_3(PO_4)_2$ and $Ba_5(PO_4)_3OH$. By precisely adjusting the pH values, micro-/nano-spheres of $BaHPO_4$, nanoparticles of $Ba_3(PO_4)_2$ and $Ba_5(PO_4)_3OH$ with different sizes could be altered. A particular mechanism of action for pH values was described in the phases and morphologies forming process, meanwhile, the different absorption/desorption abilities of CA in different pH conditions and its molecular space-specific were considered to effect much. Interestingly, the as-synthesized three hosts were all found to emit blue light in a broad band from 380 to 625 nm for the first time, for which the complex ions luminescence mode was proposed. For comparison, $Ba_3(PO_4)_2$ was also prepared by CSS, and the photoluminescence spectrum showed a blue shift. The small volume effect, interface and surface effect of nanomaterials were used to interpret it. These phenomena are conducive to the potential application of $Ba_3(PO_4)_2$ host in n-UV conversion tri-color phosphors. Furthermore, the decay lifetimes of $BaHPO_4$, $Ba_5(PO_4)_3OH$, HT-$Ba_3(PO_4)_2$ and CSS-$Ba_3(PO_4)_2$ were determined to be 13.05, 169.64, 12.25 and 31.54 ns, respectively. The difference of decay lifetimes between HT-$Ba_3(PO_4)_2$ and CSS-$Ba_3(PO_4)_2$ were discussed to come from the quenching centers on the surface of nanomaterial HT-$Ba_3(PO_4)_2$ while that among nano-$BaHPO_4$, -$Ba_3(PO_4)_2$ and -$Ba_5(PO_4)_3OH$ were ascribed to the different electronic structures and transition probabilities from the excited state to ground state.

Notes and references

[a] Engineering Research Center of Nano-Geomaterials of Ministry of Education, China University of Geosciences,
Wuhan 430074, People's Republic of China
[b] Faculty of Materials Science and Chemistry, China University of Geosciences,
Wuhan 430074, People's Republic of China

*Corresponding author at: Faculty of Materials Science and Chemistry, China University of Geosciences, Wuhan 430074, China.

Tel.: +86 27 67884814; fax: +86 27 67883733.

E-mail address: yujunliang@sohu.com

1   I. Tale, *J. Lumin.*, 1979, **20**, 343-347.

2   S. Poort, H. Reijnhoudt, H. Van der Kuip and G. Blasse, *J. Alloys Compd.*, 1996, **241**, 75-81.

3   H. Liang, Y. Tao, Q. Zeng, H. He, S. Wang, X. Hou, W. Wang and Q. Su, *Mater. Res. Bull.*, 2003, **38**, 797-805.

4   F. Chen, X. Yuan, X. Xiong and L. Liu, *J. Chinese Rare Earth Soc.*, 2011, **29**, 450-454.

5   G. Li, C. Peng, C. Li, P. Yang, Z. Hou, Y. Fan, Z. Cheng and J. Lin, *Inorg. Chem.*, 2010, **49**, 1449-1457.

6   D. Yue, W. Lu, C. Li, X. Zhang, C. Liu and Z. Wang, *Nanoscale*, 2014, **6**, 2137-2145.

7   J. P. Liu, X. T. Huang, Y. Y. Li, K. M. Sulieman, X. He and F. L. Sun, *Cryst. Growth & Des.*, 2006, **6**, 1690-1696.

8   S. P. Garcia and S. Semancik, *Chem. Mater.*, 2007, **19**, 4016-4022.

9   C. Mu and J. He, *Mater. Lett.*, 2012, **70**, 101-104.

10 G. Li, C. Peng, C. Zhang, Z. Xu, M. Shang, D. Yang, X. Kang, W. Wang, C. Li and Z. Cheng, *Inorg. Chem.*, 2010, **49**, 10522-10535.

11 G. Demazeau, *Zeitschrift Fur Naturforschung B-A J. Chem. Sci.*, 2010, **65**, 999-1006.

12 L. A. Ramajo, F. Rubio-Marcos, A. D. Campo, J. F. Fernández, M. S. Castro and R. Parra, *Ceram. Int.*, 2014, **40**, 14701-14712.

13 M. Yang, H. You, Y. Zheng, K. Liu, G. Jia, Y. Song, Y. Huang, L. Zhang and H. Zhang, *Inorg. Chem.*, 2009, **48**, 11559-11565.

14 Q. Zhu, J. G. Li, R. Ma, T. Sasaki, X. Yang, X. Li, X. Sun and Y. Sakka, *J. Solid State Chem.*, 2012, **192**, 229-237.

15 C. Zhang, L. Zhang, C. Song, G. Jia, S. Huo and S. Shen, *J. Alloys Compd.*, 2014, **589**, 185-191.

16 G. Jia, H. You, M. Yang, L. Zhang and H. Zhang, *J. Phys. Chem. C*, 2009, **113**, 16638-16644.

17 S. Som, P. Mitra, V. Kumar, V. Kumar, J. J. Terblans, H. C. Swart and S. K. Sharma, *Dalton Trans.*, 2014, **43**, 9860.

18 Y. Yu, H. Wang, L. Li, Y. Chen and R. Zeng, *Ceram. Int.*, 2014, **40**, 14171-14175.

19 T. T. Lai, C. C. Chang, C. Y. Yang, S. Das and C. H. Lu, *Ceram. Int.*, 2013, **39**, 159-163.

20 S. Som, A. K. Kunti, V. Kumar, V. Kumar, S. Dutta, M. Chowdhury, S. K. Sharma, J. J. Terblans and H. C. Swart, *J. Appl. Phys.*, 2014, **115**, 193101.

21 Y. Wu, Q. Gu, G. Ding, F. Tong, Z. Hu and A. M. Jonas, *ACS Macro Lett.*, 2013, **2**, 535-538.

22 T. Reimer, I. Paulowicz, R. Roder, S. Kaps, O. Lupan, S. Chemnitz, W. Benecke, C. Ronning, R. Adelung and Y. K. Mishra, *ACS Appl. Mater. Interfaces*, 2014, **6**, 7806-7815.

23 V. Uvarov and I. Popov, *Mater. Char.*, 2013, **85**, 111-123.

24 L. Zhou and B. Yan, *J. Phys. Chem. Solids*, 2008, **69**, 2877-2882.

25 A. K. V. Raj, P. Prabhakar Rao, T. S. Sreena, S. Sameera, V. James and U. A. Renju, *Phys. Chem. Chem. Phys.*, 2014, **16**, 23699-23710.

26 H. Lai, Y. Du, M. Zhao, K. Sun and L. Yang, *Ceram. Int.*, 2014, **40**, 1885-1891.

27 C. Li, J. Yang, P. Yang, H. Lian and J. Lin, *Chem. Mater.*, 2008, **20**, 4317-4326.

28 Y. Xu, S. Xu, S. Wang, Y. Zhang and G. Li, *Dalton Trans.*, 2014, **43**, 479-485.

29 Y. K. Mishra, S. Kaps, A. Schuchardt, I. Paulowicz, X. Jin, D. Gedamu, S. Wille, A. Kovalev, O. Lupan and R. Adelung, *KONA Powder Part. J.*, 2014, **31**, 92-110.

30 Z. He, Y. Ueda and M. Itoh, *J. Cryst. Growth*, 2006, **297**, 1-3.

31 L. Cheng, H. Zhong, J. Sun, X. Zhang, Y. Peng, T. Yu and X. Zhao, *J. Rare Earths*, 2008, **26**, 211-214.

32 N. Pan, B. Wang, X. P. Wang and J. G. Hou, *J. Mater. Chem.*, 2010, **20**, 5567-5581.

33 Y. K. Mishra, S. Kaps, A. Schuchardt, I. Paulowicz, X. Jin, D. Gedamu, S. Freitag, M. Claus, S. Wille, A. Kovalev, S. N. Gorb and R. Adelung, *Part. & Part. Syst. Char.*, 2013, **30**, 775-783.

34 S. D. Zhu, G. S. Zhou, R. Cai, Y. Han and W. Tian, *Chinese Heat Treat. Tech. & Equip.*, 2010, **31**, 1-5.

35 J. L. Zhang, G. Y. Hong. *Chinese J. Lumin.*, 2005, **26**, 285-293.

36 T. Skibiński, S. M. Kaczmarek, G. Leniec, T. Tsuboi, Y. Nakai, M. Berkowski, Z. Kowalski and W. Huang, *J. Cryst. Growth*, 2014, **401**, 802-806.

37 X. C. Chu, Y. N. Xu and L. T. Li, *J. Mater. Sci. Mater. Electron.*, 2014, **25**, 2601-2604.

38 A. Barros, R. Deloncle, J. Deschamp, P. Boutinaud, G. Chadeyron, R. Mahiou, E. Cavalli and M. G. Brik, *Opt. Mater.*, 2014, **36**, 1724-1729.

39 V. Kumar, A. K. Bedyal, J. Sharma, V. Kumar, O. M. Ntwaeaborwa and H. C. Swart, *Appl. Phys. A*, 2014, **116**, 1785-1792.

40 Z. Xia, Y. Liang, W. Huang, D. Yu, M. Zhang and M. Tong, *Ceram. Int.*, 2013, **39**, 7097-7100.

41 C. J. Ballhausen and A. D. Liehr, *J. Mol. Spectrosc.*, 1958, **2**, 342-360.

42 Z. Xia, Y. Liang, D. Yu, M. Zhang, W. Huang, M. Tong, J. Wu and J. Zhao, *Opt. & Laser Tech.*, 2014, **56**, 387-392.

43 A. I. Becerro, S. Rodríguez-Liviano, A. J. Fernández-Carrión and M. Ocaña, *Cryst. Growth & Des.*, 2013, **13**, 526-535.

44 D. Li, S. Z. Lu, J. S. Zhang, J. Y. Liu, H. Y. Wang, L. D. Sun and S. H. Huang, *Chinese J. Lumin.*, 2002, **21**, 134-138.